Whole-brain anatomical networks: Does the choice of nodes matter?

Andrew Zalesky [a,b,*], Alex Fornito [a,c], Ian H. Harding [a], Luca Cocchi [a], Murat Yücel [a,d], Christos Pantelis [a], Edward T. Bullmore [c]

[a] Melbourne Neuropsychiatry Centre, Department of Psychiatry, The University of Melbourne and Melbourne Health, Australia
[b] Department of Electrical and Electronic Engineering, Melbourne School of Engineering, The University of Melbourne, Australia
[c] Behavioural and Clinical Neuroscience Institute, University of Cambridge, Department of Psychiatry, Herchel Smith Building for Brain and Minds Sciences, Cambridge Biomedical Campus, Cambridge, UK
[d] Orygen Youth Health Research Centre, Centre for Youth Mental Health, The University of Melbourne, Australia

ARTICLE INFO

ABSTRACT

Whole-brain anatomical connectivity in living humans can be modeled as a network with diffusion-MRI and tractography. Network nodes are associated with distinct grey-matter regions, while white-matter fiber bundles serve as interconnecting network links. However, the lack of a gold standard for regional parcellation in brain MRI makes the definition of nodes arbitrary, meaning that network nodes are defined using templates employing either random or anatomical parcellation criteria. Consequently, the number of nodes included in networks studied by different authors has varied considerably, from less than 100 up to more than 10^4. Here, we systematically and quantitatively assess the behavior, structure and topological attributes of whole-brain anatomical networks over a wide range of nodal scales, a variety of grey-matter parcellations as well as different diffusion-MRI acquisition protocols. We show that simple binary decisions about network organization, such as whether small-worldness or scale-freeness is evident, are unaffected by spatial scale, and that the estimates of various organizational parameters (e.g. small-worldness, clustering, path length, and efficiency) are consistent across different parcellation scales at the same resolution (i.e. the same number of nodes). However, these parameters vary considerably as a function of spatial scale; for example small-worldness exhibited a difference of 95% between the widely-used automated anatomical labeling (AAL) template (~100 nodes) and a 4000-node random parcellation ($\sigma_{AAL} = 1.9$ vs. $\sigma_{4000} = 53.6 \pm 2.2$). These findings indicate that any comparison of network parameters across studies must be made with reference to the spatial scale of the nodal parcellation.

© 2009 Elsevier Inc. All rights reserved.

Introduction

Modeling the whole human brain as a network, the so-called human connectome (Sporns et al., 2005), has gained significant interest in the last few years. Two distinct types of whole brain networks have now been empirically mapped using different magnetic resonance imaging (MRI) modalities: *anatomical* networks and *functional* networks.

An anatomical brain network is derived from diffusion-MRI (d-MRI) and models the axonal fiber bundles that support information transfer between spatially isolated grey-matter regions. Structural connectivity is therefore often referred to as anatomical or physical connectivity and can be mapped *in vivo* with tractographic methods. On the other hand, a functional brain network is typically derived from measures of functional connectivity; in particular, correlated activity between regions over time, assessed using either resting-state

functional-MRI (rs-fMRI), magnetoencephalography (MEG) or electroencephalography (EEG).

Efforts have been devoted to elucidating the topological properties of human brain networks in both health and disease. A summary of some studies is shown in Table 1.

Topological properties can be mathematically analyzed by characterizing the brain as an undirected graph, where each region-of-interest composing a grey-matter parcellation serves as a node and each link represents some statistical measure of association, such as correlations in physiological time series; interconnecting axonal fiber pathways; or inter-regional covariance in anatomical parameters such as cortical thickness (Bullmore et al., 2009).

The two most ubiquitous topological properties that brain networks have been tested for are scale-freeness in nodal distribution (Amaral et al., 2000) and small-worldness (Watts and Strogatz, 1998). It has been shown that the topology of both anatomical and functional brain networks exhibit small-world properties (Bullmore et al., 2009). Such networks are characterized by a high degree of locally clustered, cliquish, connectivity and low mean path length (i.e. nodes can connect with each other through only a few hops). Some studies have

* Corresponding author. Melbourne Neuropsychiatry Centre, University of Melbourne, Alan Gilbert Building, 161 Barry Street, Melbourne, VIC, Australia. Fax: +613 9348 0469.
E-mail address: azalesky@unimelb.edu.au (A. Zalesky).

Table 1
Nodal scale and parcellation across some studies of human brain networks, segregated according to imaging modality.

Study	Scale	Parcellation
rs-fMRI		
Achard et al., 2006	90	AAL
Achard and Bullmore, 2007	90	AAL
Eguiluz et al., 2005[a]	140,000	Voxel-based
Van den Heuvel et al., 2008	10,000	Voxel-based
Liu et al., 2008	90	AAL
Salvador et al., 2005c	90	AAL
Salvador et al., 200b	90	AAL
Wang et al., 2009a	90 vs. 70	AAL vs. ANIMAL
d-MRI		
Gong et al., 2009	78	AAL
Hagmann et al., 2007	500–4000	Gry/Wht. Surf.
Hagmann et al., 2008	998	Gry/Wht. Surf.
Itturia-Medina et al., 2008a	71	IBASPM
Itturia-Medina et al., 2008b	90	AAL
EEG		
Micheloyannis et al., 2006	28	Scalp sensors
Stam et al., 2007	21	Scalp sensors
MEG		
Bassett et al., 2006	275	Scalp sensors
Deuker et al., 2009	204	Scalp sensors
Stam, 2004	126	Scalp sensors
Anatomical-MRI		
Bassett et al., 2008	104	Pick Atlas
He et al., 2007, 2008	54	Jacob Atlas
d-MRI vs. f-MRI		
Honey et al., 2009	998 and 68	Gry/Wht. Surf.
Park et al., 2008	73	AAL
Skudlarski et al., 2008	5000	Voxel-based
Zalesky and Fornito, 2009	70	AAL

[a] Finger tapping task, rather than resting-state. *AAL* = automated anatomical labeling atlas; *Gry/Wht. Surf.* = random parcellation of the two-dimensional grey-white matter interface; *Voxel-based* = each grey-matter voxel serves as a distinct node; *ANIMAL* = automated gross anatomy parcellation owing to Collins et al., 1995; IBASPM, see Alemán-Gómez et al., 2006.

also claimed that the brain is scale-free (e.g. (Eguiluz et al., 2005; Van den Heuvel et al., 2008), though this view is disputed (e.g. Achard et al., 2006; Gong et al., 2009). Scale-freeness implies the existence of a few highly connected hub nodes, which endow a scale-free network with superior tolerance to random node failures (Albert et al., 2000; Kaiser et al., 2007). Recent studies have demonstrated these networks measures are altered in the diseased brain (e.g. He et al., 2008, 2009; Liu et al., 2008; Wang et al., 2009b).

At the microscopic scale, nodes composing a neural network naturally correspond to individual neurons. However, at the macroscopic scale, it is unclear how grey-matter should be parcellated in order to define a set of nodes, and at what *scale* this parcellation should be performed. The lack of a natural correspondence between network nodes and grey-matter regions-of-interest has resulted in the analysis of brain networks across a range of nodal scales spanning three orders of magnitude, from less than 10^2 nodes, up to more than 10^5. The scale of a parcellation can affect regional connectivity estimates, particularly in anatomical networks, as exemplified in Fig. 1. This figure shows an example of a forking U-fiber that is poorly characterized due to the use of a too coarse parcellation.

Most studies have utilized a subset of the 90 non-cerebellar regions-of-interest composing the automated anatomical labeling (AAL) parcellation atlas (Tzourio-Mazoyer et al., 2002) to serve as nodes (see Table 1). In the case of functional connectivity, (Wang et al., 2009a) statistically tested differences in the topological properties of an AAL-based network with a network based on an 70-node parcellation. While both networks exhibited robust small-world attributes and an exponentially truncated power law degree distribution, several topological parameters were found to exhibit significant variations across the two networks.

The substantial disparity in parcellation scales across different studies raises a question: *Does scale matter?* Since an underlying neuronal/axonal network is not necessarily endowed with the same properties as its macroscopic approximation, do claims of the form "human brain network shown to exhibit topological property *X*" need to be interpreted with respect to scale? For example, the discrepancy between Eguiluz et al., 2005; Van den Heuvel et al., 2008 versus Achard et al., 2006; Gong et al., 2009 (i.e. power law nodal distribution versus exponentially truncated power law) may be attributable to the orders of magnitude difference in scales considered.

This paper seeks to systematically evaluate the dependence of whole-brain anatomical networks over a range of nodal scales, a variety of grey-matter parcellations as well as different diffusion-MRI acquisition protocols. To this end, networks were analyzed across scales ranging from 100 to 4000 nodes. For each scale, 100 random parcellations of grey-matter were generated. Two distinct tractographic methods were then used to determine which pairs of nodes were anatomically connected.

A variety of local and global topological properties were computed for each of the 100 networks, including small-worldness, path length, clustering coefficient, nodal degree distribution, efficiency and betweenness centrality. The variation of each topological parameter across the 100 networks was then assessed to evaluate the discrepancy in parameter estimates that can be solely attributable to the choice of parcellation. Quantifying parcellation-driven discrepancies is important because the choice of parcellation is usually arbitrary or random.

It was found that topological properties vary markedly with scale. For example, if one experimenter uses the AAL template, while another uses a random 4000-node template, the value of small-worldness measured by the two experimenters will be discrepant by approximately 95% ($\sigma_{ALL} = 1.9$ vs. $\sigma_{4000} = 53.6 \pm 2.2$). Although small-world attributes were found at all scales, the extent of small-worldness was found to increase as scale is made finer, resulting from a large increase in clustering. Exponential nodal degree distributions were also found at all scales. These findings suggest scale does not matter if the experimenter simply seeks a yes/no determination about whether or not a network is small-world or scale-free, but scale does matter if the experimenter seeks to *quantify* the extent to which the network exhibits these topological properties. The variation in
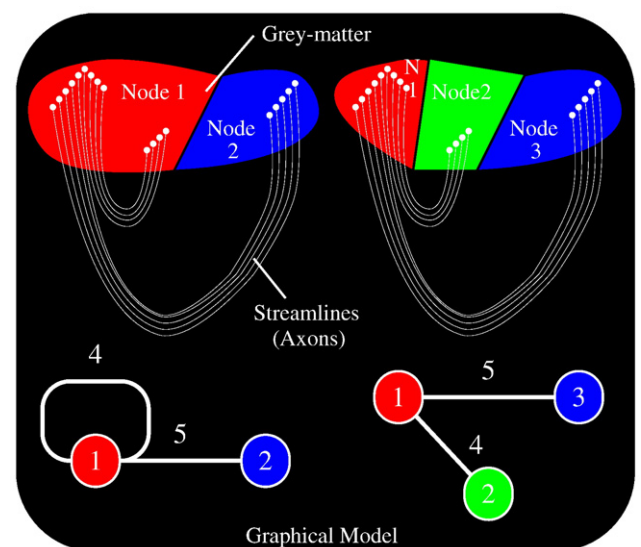
Fig. 1. Example parcellation of a forking U-fiber. The leftmost parcellation is too coarse and fails to characterize the left branch of the fork. In a graphical model, the left branch manifests as a self-loop about node 1. The rightmost parcellation is however fine enough to characterize both branches. The weight assigned to each link corresponds to the total number of intersecting streamlines.
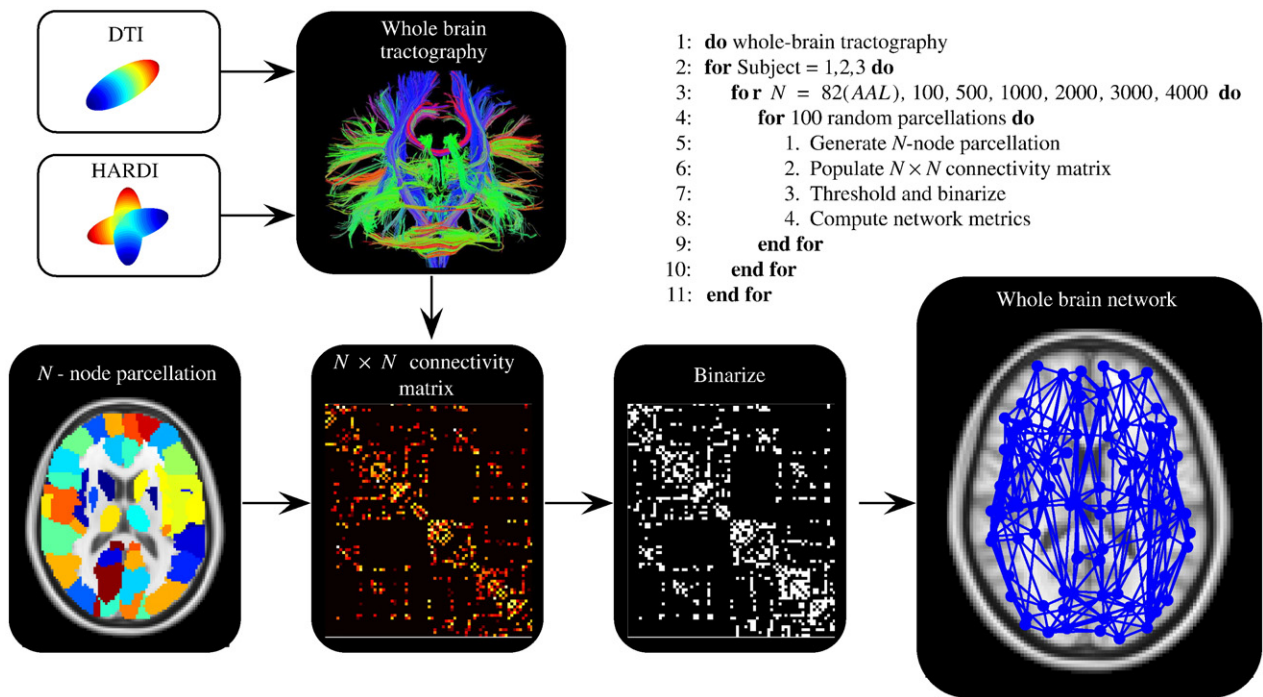
Fig. 2. An overview of the processing pipeline. The example network shown corresponds to DTI tractography in subject 1 and the 82-node AAL parcellation. The adjacency matrix is ordered such that all left-hemisphere nodes occupy the first 41 rows. Therefore, the two strongly connected sub-blocks along the diagonal exclusively correspond to intra-hemispheric connectivity, while the two off-diagonal blocks correspond to inter-hemispheric connectivity.

topological properties for networks of the *same* scale, but with different nodal parcellations was found to be more subtle (<3%).

Methods

An overview of the processing pipeline is shown in Fig. 2. Each of the ensuing subsections is dedicated to a particular stage of the pipeline.

Data acquisition and pre-processing

A total of 6 d-MRI data sets were acquired; in particular, a 252-direction ($b = 4000$ s/mm^2) high-angular resolution diffusion imaging (HARDI) protocol was acquired in 3 healthy controls (F, 32; M, 23; M, 25) followed by a 60-direction ($b = 2000$ s/mm^2) diffusion tensor imaging (DTI) protocol acquired in the same 3 subjects. Acquisition of both HARDI and DTI data sets enabled comparison of networks derived from tractographic methods that do and do not model the presence of crossing-fibers.

All data sets were acquired with a spin-echo EPI sequence using a Siemens Trio 3.0 Tesla scanner (Siemens, Erlangen) located at the Royal Children's Hospital, Melbourne, Australia. Foremost, 60 gradient directions with $b = 2000$ s/mm^2 were acquired over a 128×128 image matrix (256×256 mm^2 field of view, TE = 99 ms, TR = 8720 ms) at 64 consecutive axial slices of thickness 2 mm, thus resulting in voxels dimensions of 2 mm isotropic. The gradient directions were uniformly distributed on the half-sphere. This constituted the DTI protocol.

Immediately subsequent to the completion of the DTI protocol, 252 gradient directions $b = 4000$ s/mm^2 were acquired over a 128×128 image matrix (282×282 mm^2 field of view, TE = 120 ms, TR = 7550 ms) at 48 consecutive axial slices of thickness 2.2 mm, thus resulting in voxel dimensions of 2.2 mm isotropic. The gradient directions were obtained from the vertices of a fivefold tesselated icosahedron projected onto the sphere. This constituted the HARDI protocol, which was modeled on the protocol developed in Tuch (2004).

Several T_2 non-diffusion weighted images were acquired at regular intervals during both protocols. The total time of acquisition per subject was approximately 40 mins. The mean SNR of the diffusion-weighted images was 27.6 ± 0.8 for the DTI acquisition and 14.3 ± 0.4 for HARDI, where the standard deviation was computed over all diffusion weighted images.

To correct for slight head motion, each diffusion weighted image was registered to a representative T_2 image using a rigid-body transform. Each representative T_2 image was then registered to MNI space using a 12-parameter affine transform, and the transform was stored for later use. The diffusion weighted images remained in native space. Registration was performed using the algorithm in Jenkinson et al. (2002).

Parcellation

Grey-matter was randomly parcellated into *N* contiguous regions-of-interest using a simple parcellation algorithm that was particularly developed for this purpose. Each region-of-interest was required to serve as a distinct node (vertex) in a graphical brain model.

The parcellation algorithm was developed to minimize the variation in nodal volume and was performed at voxel resolution. The value of *N* and a binary grey-matter mask (binarized AAL template) was provided as input to the algorithm.

The algorithm operates as follows: *N* grey-matter seed voxels are chosen at random, each of which corresponds to the first voxel to be classified as belonging to each of the *N* nodes. All other grey-matter voxels remain unclassified. The strategy is to incrementally 'grow' each node voxel-by-voxel until every grey-matter matter voxel has been assigned to exactly one node. At each iteration of the growth phase, a new voxel is assigned to the node with the smallest volume. If two or more nodes are of equally small volume, one is chosen randomly. The new voxel that is assigned at each iteration is selected so that the surface area (i.e. voxel faces) between it and the chosen node is maximal. A voxel cannot be assigned to a node with which it shares no surface area. If two or more voxels are equally strong neighbors, the voxel that is closest in distance to the current center of mass of the node is chosen. Any further ties between voxels are

broken randomly. Note that the growth of a node may be stunted if all the voxels with which it shares a surface have already been assigned to other nodes.

Akin to Hagmann et al., 2007, each node was constrained to lie within the periphery of one and only one AAL region-of-interest. This constraint precluded the formation of nonsensical nodes, such as nodes that encompass both hemispheres. To enforce this constraint, the parcellation algorithm was invoked separately for each AAL region-of-interest. In particular, the proportion of streamline endpoints residing in each AAL region-of-interest was first tallied. An AAL region-of-interest comprising a proportion p of the total number of endpoints was then parcellated into pN nodes. This ensured more nodes were assigned to regions-of-interest at which many axonal pathways terminate. See Appendix for pseudocode of the entire parcellation algorithm.

To serve as a grey-matter mask, an 82-node version of the AAL template was binarized (i.e. subcortical nuclei and cerebellum were omitted). The standard AAL template comprises 116 nodes; however, all cerebellar and sub-cortical regions-of-interest were omitted because the HARDI acquisition yielded only partial coverage of the cerebellum, and accurate grey-matter segmentation in subcortical regions can be problematic. Since the AAL incorporates significant portions of white-matter, this template was contracted by a few voxels in regions where excessive non-cortical coverage was evident. This contracted AAL-based binary grey-matter mask was registered to native space using the inverse of the transforms stored during the preprocessing stage. Since the aim herein is to characterize topological attributes as a *distribution* across all random parcellations of a fixed scale, N, it was not necessary to ensure the same nodal parcellation was used for each subject. It was therefore possible to perform parcellation in native space.

Tractography

For each DTI acquisition, a tensor was fitted to each voxel using weighted linear least squares (Salvador et al., 2005a). The orientation of the eigenvector with largest eigenvalue was assumed to correspond to the local orientation of any underlying axonal fiber bundle. While this assumption is entrenched in DTI studies, it is known to yield erroneous orientations in the case of crossing fibers (Hess et al., 2006). The eigenvector with largest eigenvalue is henceforth referred to as the *principal eigenvector*.

For each white-matter voxel, a streamline was initialized from each of the two opposing directions of the principal eigenvector. Each streamline was propagated in fixed increments of 1 mm using the FACT algorithm (Mori et al., 1999). Propagation was terminated if either a minimum angle threshold of 50° was violated or if a voxel was encountered with fractional anisotropy below 0.2. At each increment, the direction of propagation was parallel to the orientation of the eigenvector closest to the current streamline endpoint. In subsequent analysis, the two opposing streamlines initialized from each white-matter voxel were joined at their point of initialization and considered to be a single streamline. The coordinates of each streamline were stored for later use.

For each HARDI acquisition, the higher angular resolution and higher gradient strength enabled fitting an orientation distribution function (ODF) to each voxel. Fitting an ODF can potentially capture the presence of multiple fiber orientations. An ODF was analytically fitted to each voxel using q-ball reconstruction with spherical harmonic basis functions (Hess et al., 2006). The appeal of q-ball reconstruction (Tuch, 2004) relative to alternative ODF reconstruction techniques such as spherical deconvolution (Tournier et al., 2005) is that q-ball is model free and thus does not require estimation of a response function.

For tractographic purposes, each ODF was discretized along 181 directions spanning the half-sphere, yielding an angular sampling resolution of $10.85° \pm 0.97°$. Local maxima of each discretized ODF were then computed and assumed to correspond to the local orientation of any underlying axonal fiber bundles. For each white-matter voxel, a streamline was initialized from each of the two opposing directions of each local maxima. Streamlines were propagated using precisely the same algorithm and termination criteria used for DTI tractography. In cases of multiple local maxima, the direction of propagation was chosen to proceed parallel to the particular local maximum which was most closely aligned with the current streamline direction. The claimed advantage of this tractographic approach (e.g. Hagmann et al., 2007) relative to conventional DTI tractography is that streamlines can accurately navigate through fiber intersections and other complex fiber geometries that are poorly modeled with a single compartment fit.

While several alternative tractographic methods have been customized to network mapping (e.g. Hagmann et al., 2007; Jbabdi et al., 2007; Itturia-Medina et al., 2008a; Zalesky, 2008; Zalesky and Fornito, 2009), this study utilized the DTI and HARDI versions of FACT streamline tracking (Mori et al., 1999) described above. Local greediness is a key disadvantage of streamline tracking that has been shown to obstruct the reconstruction of long fiber bundles (e.g. transcallosal pathways) due to noise corruption (Zalesky, 2008). While globally optimal approaches address this disadvantage, they are more computationally demanding.

Tractographic maps were viewed with TrackVis (http://www.trackvis.org).

Graph construction

Graph construction involved utilizing tractographic results and an N-node parcellation as input to populate an $N \times N$ connectivity matrix, formally known as an adjacency matrix. An adjacency matrix completely specifies the structure of a graph and is denoted herein as $\mathbf{A}$.

A streamline was considered *usable* if and only if it intersected grey-matter. Any unusable streamlines were culled from the set of all streamlines and given no further consideration. Specifically, any streamline that was wholly constrained to white-matter, the sub-cortex, the cerebellum or a combination thereof was culled. Culling is a necessary step to eliminate spurious streamlines that do not interconnect distinct grey-matter regions. Streamlines that were less than 5 mm in length were also culled. Fig. 3 shows the set of all, culled and usable streamlines.

Table 2 shows that while HARDI tractography yielded more streamlines in total compared to DTI, many of these extra streamlines were spurious. Nevertheless, as exemplified in Fig. 3, HARDI yielded significantly stronger inter-hemispheric connectivity.
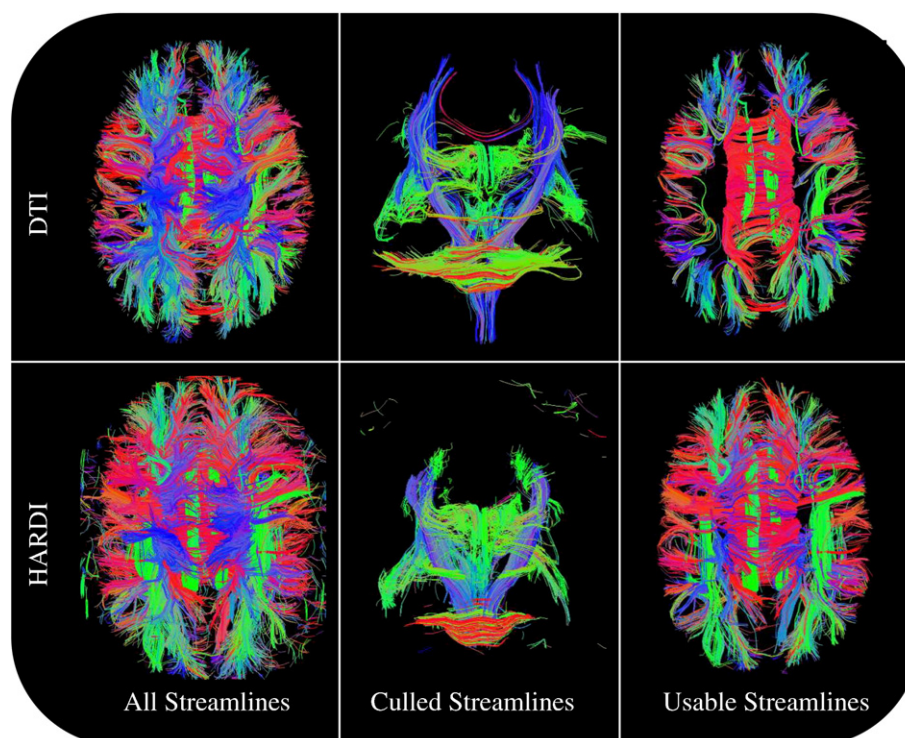
Let S be the set of all usable streamlines and let $s \in S$ denote a particular streamline, where $s = (x_1, x_2,...,x_K)$, $x = (x, y, z)$, is the ordered set of coordinates defining the streamline's trajectory. Furthermore, let $G(n) = (x_1, ..., x_{J_n})$, $n = 1, 2,..., N$, denote the grey-matter volume encapsulated by the nth node composing an N-node parcellation, where J_n is the number of voxels encapsulated.

Each streamline was decomposed into three contiguous segments $\mathbf{s} = (\mathbf{U}, \mathbf{s}_{white}, \mathbf{V})$, where $\mathbf{s}_{white}$ contains all the white-matter coordinates, while $\mathbf{U}$ and $\mathbf{V}$ contain the grey-matter coordinates at each of the streamline's two extremities. For streamlines constrained to grey-matter, $\mathbf{s}_{white} = \varnothing$.

Let u be the first coordinate in the set $\mathbf{U}$ and let $\mathbf{v}$ be the last coordinate in the set $\mathbf{V}$ (i.e. $\mathbf{u}$ and $\mathbf{v}$ are the streamline endpoints). An adjacency matrix was populated such that for $i \neq j$,

$$\mathbf{A}_{i,j} = \sum_{s \in S} \mathbf{I}_{\{u \in G(i)\}} \mathbf{I}_{\{v \in G(j)\}} + \mathbf{I}_{\{u \in G(j)\}} \mathbf{I}_{\{v \in G(i)\}},$$

where the indicator is defined such that $\mathbf{I}_{\{\mathbf{u} \in G(i)\}} = 1$ if the endpoint coordinate $\mathbf{u}$ resides within the volume $G(i)$, otherwise $\mathbf{I}_{\{\mathbf{u} \in G(i)\}} = 0$. In

Fig. 3. The set of all, culled and usable streamlines. Streamlines representing the cortico-spinal tract and cerebellum were culled. Streamlines less than 5 mm in length (prevalent in HARDI) were considered spurious and also culled. The set of usable streamlines characterize cortico-cortical connectivity. Axial orientation: bottom of page is posterior. Coronal orientation: coming out of page is anterior.

words, the above equation stipulates that element $\mathbf{A}_{i,j}$ is populated with the total number of usable streamlines that traverse the volume encapsulated by both nodes i and j. This resulted in an adjacency matrix that defines a simple, undirected and weighted graph.

Since some topological properties of a weighted graph are ill-defined, each graph was binarized simply by assigning unity weight to all non-zero entries. This resulted in a sparse, un-weighted graph comprising one giant connected component. For the finest scales considered, some nodes were disconnected from the giant component. No cases were encountered in which more than 3% of the nodes were disconnected. Sparsity (ratio of nodes-to-links) ranged between approximately 5 and 700, where the finest scales considered yielded the most sparse networks. A discussion of this large difference in sparsity is given in Section 4.

Unlike rs-fMRI network modeling, a thresholding process was not necessary because the weighted adjacency matrix is intrinsically sparse, since most node pairs are not interconnected by even a single streamline. In contrast, with rs-fMRI, a non-zero, albeit a possibly small functional correlation is found between all network nodes, hence necessitating the use of a thresholding procedure to yield a sparse adjacency matrix.

Several alternative approaches for populating an adjacency matrix have been advocated. In (Gong et al., 2009), streamline propagation is terminated at the *first* point grey-matter is encountered and only this point dictates the structure of the adjacency matrix. The advantage of this approach is the avoidance of streamline propagation deep within grey-matter, which can potentially be unreliable due to the isotropy of grey-matter. The disadvantage is that a node remains disconnected if it does not reside on the grey-white matter boundary (i.e. 'landlocked' between other nodes). With this approach, it must therefore be ensured that all nodes composing a parcellation template are carefully defined to avoid landlocked regions-of-interest. Note that the concept of a landlocked node does not apply to approaches in which streamlines can continue to propagate within grey-mater.

Topological properties

Several local and global topological properties were evaluated; specifically: average path length, clustering coefficient, small-worldness (Watts and Strogatz, 1998), nodal degree distribution (Amaral et al., 2000), local efficiency and global efficiency (Kaiser and Hilgetag, 2006; Latora and Marchiori, 2001) and betweenness centrality (Freeman, 1979; Newman, 2003). Each of these properties and their biological significance has been defined and discussed in detail elsewhere (e.g. (Bullmore et al., 2009; Bullmore and Sporns, 2009; Sporns et al., 2004)). Standard formulae (Newman, 2003) were utilized to compute each measure. To avoid the computational nuisance in dealing with infinite path lengths, the path length of any node that was disconnected from the giant component was set to the maximum path length between any pair of nodes in the giant component.

Let c_G denote the average clustering coefficient and let l_G denote the average path length of a graph G. To test for small-worldness of G, the σ-ratio, $\sigma = \gamma/\lambda$ was evaluated, where $\gamma = c_G/c_R$, $\lambda = l_G/l_R$ and R represents a 'random' graph that is equivalent to G. According to the σ-ratio, G was diagnosed as small-world if $\gamma > 1$ and $\lambda \approx 1$. These two conditions were abbreviated to the single test $\sigma > 1$.

In many studies, a random graph R was considered equivalent to G if and only if R and G exhibit an identical nodal degree distribution. To

Table 2
Summary of streamline statistics segregated according to subject and acquisition.

	Subject 1		Subject 2		Subject 3	
	DTI	HARDI	DTI	HARDI	DTI	HARDI
Total [×10³]	100	211	101	160	118	208
Usable [×10³]	28	38	32	36	39	44
Usable %	28	18	32	23	33	21
Mean [mm]	21.5	29.6	25.5	30.3	27.0	32.7

compute a random graph R satisfying this equivalence criterion, the iterative randomization algorithm presented in Maslov and Sneppen (2002) or the sequential algorithm in Bayati et al., 2007 can be invoked. In Achard et al. (2006); Van den Heuvel et al. (2008); Liu et al. (2008), the algorithm in Maslov and Sneppen (2002) was reinvoked M times to compute M random graphs $R_1,...,R_M$ equivalent to G, thereby affording the Monte-Carlo approximation $c_R = \langle c_{R_1},...,c_{R_M} \rangle$ and $l_R = \langle l_{R_1},...,l_{R_M} \rangle$.

Approximating c_R and l_R as such was intractable for the large graphs that were considered herein. Instead, well-known analytical results for an equivalent Erdős–Rényi random graph; namely, $c_R = d/N$ and $l_R = \log N/\log d$ were used, where d denotes average nodal degree. The disadvantage of this analytical approach is that it was

necessary to relax the definition of equivalence between G and R; specifically, it was no longer insisted that G and R exhibit an identical nodal degree distribution, but only identical *average* nodal degree.

We assessed the consequence of matching average nodal degree instead of the entire degree distribution by estimating the σ-ratio for a few computationally tractable cases using the randomization algorithm devised in Bayati et al. (2007) to generate 500 random graphs. This algorithm yields normalizing graphs that are matched in degree distribution. It was found that matching the average nodal degree (i.e. Erdős–Rényi normalization) yielded a more conservative estimate of the σ-ratio compared to matching the entire degree distribution. Specifically, in the case of the AAL, Erdős–Rényi normalization yielded $\sigma = 2.6$, 2.5 and 2.5 for each of the three
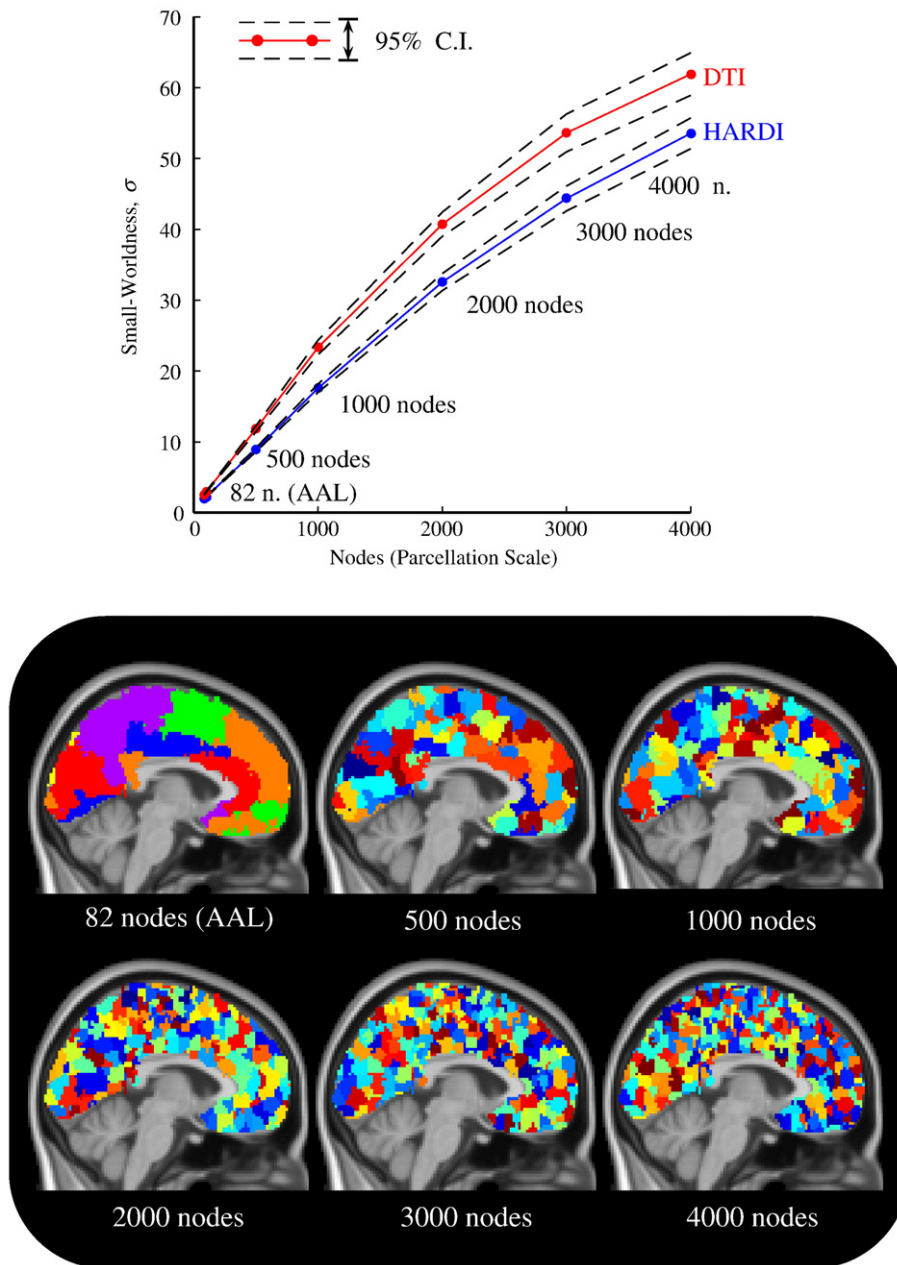
Fig. 4. Small-worldness (σ-ratio) as a function of the number of nodes. Each data point was computed as follows: for each acquisition and for each of 100 random parcellations, a brain network was constructed and its σ-ratio computed. The mean and standard deviation of the 100 σ-ratios was computed separately for each of the 6 acquisitions (3 HARDI and 3 DTI), thereby yielding 6 means and 6 standard deviations. Finally, the means and standard deviations were averaged across the 3 DTI acquisitions and separately across the 3 HARDI acquisitions, thereby yielding two data points (blue and red) for each nodal scale. The null hypothesis $\sigma_{DTI} = \sigma_{HARDI}$ was rejected with $p < 10^{-8}$ for all nodal scales considered. Also shown is a sagittal representation of some arbitrarily chosen parcellations of varying scale.

subjects (DTI acquisition), while matching the full degree distribution yielded $\sigma = 3.0 \pm 0.2$, 2.9 ± 0.1 and 3.7 ± 0.1. This suggests Erdős–Rényi normalization yields a stricter definition of small-worldness.

To test for scale-freeness of a graph comprising N nodes, the degree of each node was ranked from $1, \ldots, N$ such that the node with highest degree was ranked with the index 1 and the node with the lowest degree was ranked with the index N. Nodal rank as a function of degree was then plotted on a set of doubly logarithmic axes. A roughly linear rank-degree plot is indicative of a scale-free degree distribution, since a scale-free degree distribution d_i is defined such that $d_i = c y_i^{-\alpha}$, where y_i is the rank of d_i, and c and α are constants. Since $\log(d_i) = \log(c) - \alpha \log(y_i)$, plotting rank versus degree on doubly logarithmic axes yields a line of slope $-\alpha$. Rank-degree plots were opted for in favor of the more common frequency-degree plots utilized in Achard et al. (2006); Gong et al. (2009); Hagmann et al. (2007); Van den Heuvel et al. (2008). This is because the binning process involved in generating a frequency-degree plot has been shown to introduce artifacts (see (Liu et al., 2005)).

Evaluation

The processes detailed in Sections 2.2–2.5 were repeated 100 times for parcellations of scale $N = 82$ (AAL), 100, 500, 1000, 2000, 3000, 4000 and for each of the 6 acquisitions (3 HARDI and 3 DTI). Therefore, a total of $100 \times 6 \times 6 = 3600$ networks were mapped, represented as a graph and evaluated for the presence of several topological properties.

For each nodal scale, N, and for each subject, the mean and standard deviation of each measure was computed across the 100 networks (i.e. 100 random parcellations of the same scale). In this way, each topological attribute was characterized as a distribution across all parcellations of a fixed scale N. This distribution represents the variation of a measure across different parcellations of the *same* scale.

Of equal importance was the variation of a measure across parcellation templates of *different* scale. This kind of variation is useful in determining the compatibility of the results reported in studies utilizing significantly different scales, for example, Skudlarski et al. (2008) (5000-node) versus Gong et al. (2009) (78-node AAL). To this end, the above described mean and standard deviation was plotted for each global measure as a function of scale. To avoid cluttering, rather than plotting a trace for each subject, the means and standard deviations were averaged across the 3 DTI acquisitions and separately across the 3 HARDI acquisitions, thereby yielding two distinct traces that enable explicit comparison of HARDI and DTI. This across subject averaging also assists in suppressing the effects of variation owing to individual anatomical differences.

The distribution of relative error between two distinct parcellations of the same scale was computed for each global measure and the mean of this distribution was tabulated. The distribution of relative error was constructed by enumerating all $\binom{100}{2} = 4950$ pairs of parcellations from the pool of 100 and computing the relative error between each pair for the particular measure of interest. The mean of this distribution was then computed across the 4950 pairs to yield the expected relative error at a given scale. This enables quantitative evaluation of questions of the form: if an experimenter computes small-worldness with respect to a particular N-node parcellation, while a second experimenter performs the same computation with respect to an alternative N-node parcellation, what is the expected difference (relative error) between the values of small-worldness computed by both experimenters?

Results

The first topological property considered was small-worldness, $\sigma = \gamma/\lambda$. Fig. 4 shows small-worldness plotted as a function of the

number of network nodes. A distinct trace is shown for HARDI (blue) and DTI (red). The dashed lines correspond to 95% confidence intervals. Fig. 4 also shows a sagittal representation of some arbitrarily chosen parcellations of varying scale.

The variability in the σ-ratio is rather small across parcellations of the same scale which can be assessed by the tightness of the confidence intervals in Fig. 4. In contrast, the σ-ratio exhibits a marked increase as nodal scale is made finer. This means finer parcellations give rise to 'stronger' small-world attributes. For example, in the case of HARDI, the σ-ratio is approximately 95% greater for a 4000-node template ($\sigma = 53.6 \pm 2.2$) compared to the AAL ($\sigma = 1.9$). Therefore, a σ-ratio should be reported and compared across studies with respect to a parcellation scale.

For each nodal scale, the null hypothesis $\sigma_{DTI} = \sigma_{HARDI}$ was tested using a two-tailed Student's t-test. The standard deviations used to construct this t-test accounted for the variation of the σ-ratio across different parcellations of the same scale.

The null hypothesis $\sigma_{DTI} = \sigma_{HARDI}$ was rejected with $p < 10^{-8}$ for all nodal scales considered. Note that the null hypothesis was not
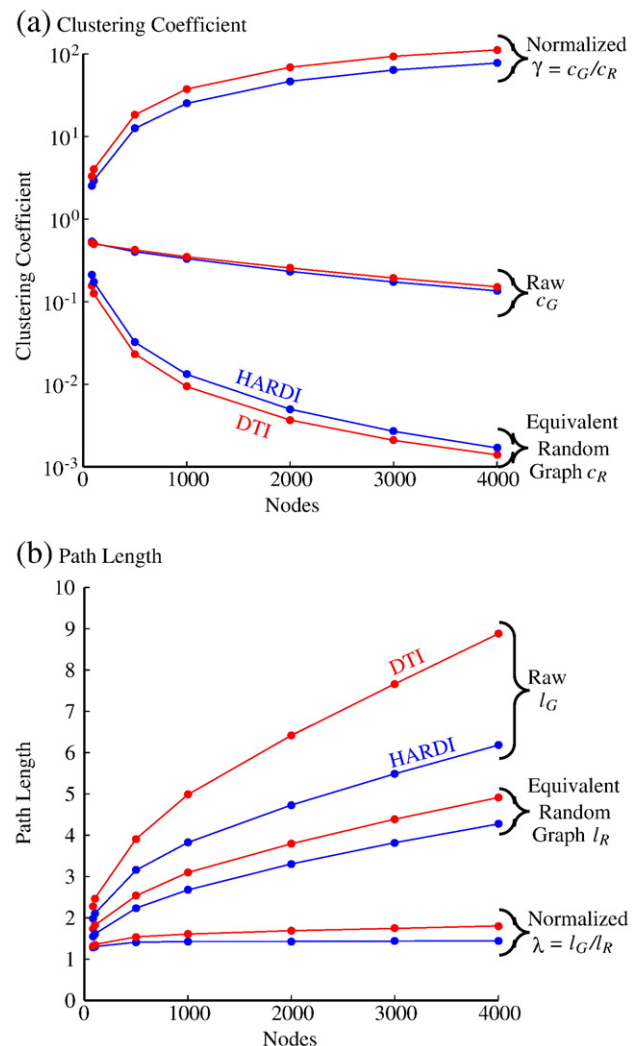
Fig. 5. Average clustering coefficient and path length (raw, G, equivalent random graph, R, and normalized value). Normalization is with respect to an equivalent Erdős–Rényi random graph with the same number of nodes and same average nodal degree. Confidence intervals were suppressed for the intervals were too small to distinguish in most cases. The discrepancy between HARDI and DTI was statistically significant with $p < 10^{-4}$ for both the raw and normalized values of l and c, and for all the scales considered.
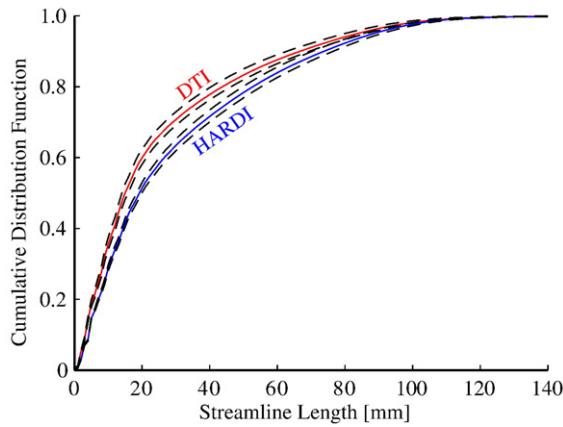
Fig. 6. Cumulative distribution function of streamline length segregated with respect to HARDI and DTI. This plot confirms HARDI tractography yields longer streamlines. For example, in the case of DTI, 78% of streamlines are less than 40 mm in length, while only 72% are less than 40 mm for HARDI.

tested for the AAL ($N = 82$), since there is no parcellation variation in this case.

Fig. 4 shows that networks owing to DTI derived tractographic maps exhibited stronger small-world attributes than their HARDI counterparts; in particular, a relatively consistent difference of approximately 8.5 was evident in the σ-ratio for all scales considered beyond 1000 nodes. Was this due to a higher clustering coefficient, γ, or a shorter average path length λ? (Since $\sigma = \gamma/\lambda$, stronger small-world attributes can be owing either to an increase in clustering, a decrease in path length or a combination of both.) To address this question, the normalized path length, $\lambda = l_G/l_R$, and the average normalized clustering coefficient, $\gamma = c_G/c_R$, were plotted as function of the number of nodes in Figs. 5a and b, respectively. These two figures adhere to precisely the same format as the plot presented in Fig. 4.

To understand the effect of normalization, the 'raw' (i.e. non-normalized) clustering coefficient, c_G, and the raw path length, l_g, was also plotted in Fig. 5. In this way, the raw clustering coefficient was explicitly decoupled from the analytically derived coefficient of the normalizing Erdős–Rényi random graph model.

Consideration of Fig. 5 shows path lengths are marginally longer in DTI relative to HARDI, however, this difference in path length is overshadowed by a significantly higher clustering coefficient in DTI. Hence, the net effect is an increase in the σ-ratio for DTI. In other
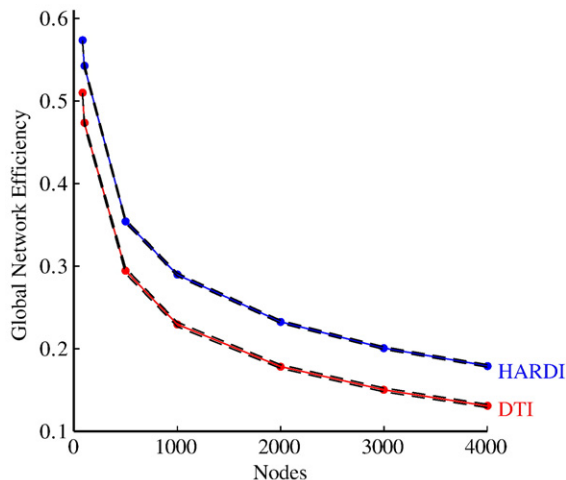
Fig. 7. Global network efficiency. The null hypothesis of equal network efficiency for HARDI and DTI was rejected with $p < 10^{-8}$ for all nodal scales considered.
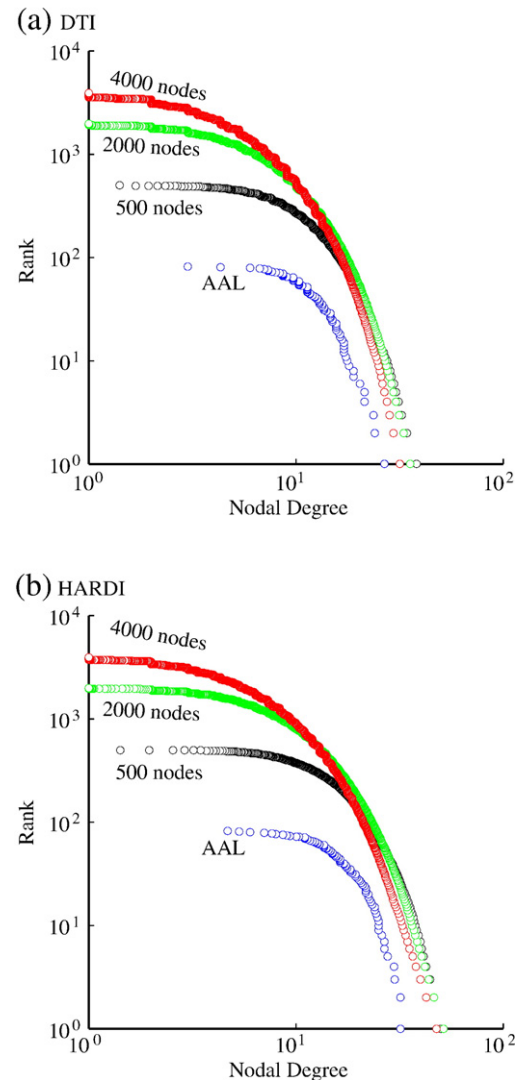
Fig. 8. Nodal rank plotted as a function of degree for DTI and HARDI. For each of 100 random parcellations, a brain network was constructed and its degree sequence ranked such that the node with largest degree was assigned a rank of one. For each rank, the mean of the corresponding nodal degree was computed across the 100 networks. This process was repeated for the three acquisitions. Therefore, a total of $100 \times 3 = 300$ networks were ranked. Rank-degree plots were then constructed based on the average across these three acquisitions.

words, DTI-derived networks exhibit slightly longer path lengths, but significantly greater clustering. Therefore, with HARDI, only a few links (streamlines) need to be traversed to travel a long distance, whereas with DTI, the presence of many short links yields high clustering but also means many links must be traversed to travel a commensurate distance. This explanation is further supported by

Table 3
Least squares fit of the three parameters underlying the exponentially truncated power law model $y_i = cd_i^{\alpha-1}e^{-d_i/k}$.

	$N = 100$	$N = 500$	$N = 2000$	$N = 4000$
DTI				
k	2.8	4.0	4.0	3.5
α	3.0	2.0	1.5	1.3
c	0.52	0.72	1.9	3.8
HARDI				
k	3.6	5.7	5.5	4.8
α	3.4	2.0	1.4	1.2
c	0.1	0.5	1.5	3.1

Table 4
Relative error, $|x - y| / \max(x, y)$, in the value of small-worldness, σ, normalized clustering coefficient, γ, and normalized path length, λ, computed across random parcellations of the same scale. Values averaged across the three DTI acquisitions.

# Nodes	Small-worldness	Clustering	Path length
82 (AAL)	0	0	0
100	$1.4 \pm 1.1\%$	$1.3 \pm 1.0\%$	$0.3 \pm 0.2\%$
500	$1.9 \pm 1.5\%$	$1.7 \pm 1.3\%$	$0.7 \pm 0.6\%$
1000	$2.3 \pm 1.9\%$	$2.0 \pm 1.6\%$	$0.8 \pm 0.6\%$
2000	$2.3 \pm 1.7\%$	$2.1 \pm 1.6\%$	$0.9 \pm 0.7\%$
3000	$2.7 \pm 2.0\%$	$2.2 \pm 1.6\%$	$1.2 \pm 1.0\%$
4000	$2.5 \pm 2.1\%$	$2.3 \pm 1.8\%$	$1.2 \pm 1.0\%$

Fig. 6, which shows the distribution of streamline lengths for HARDI is skewed towards longer streamlines relative to DTI.

It is important to remark that the expression of stronger small-world attributes does not suggest DTI has yielded a biologically truer network model of anatomical connectivity. The purpose herein is not to determine which choice yields a truer network model, but rather to draw attention to the fact that topological properties can indeed vary markedly across different tractographic methods, acquisition protocols, and parcellation scales and templates.

For coarse parcellation scales, the discrepancy in clustering and path length between DTI and HARDI is negligible, however, for a 4000-node scale, this discrepancy is approximately 31% with respect to normalized clustering (111.7 ± 4.8 versus 77.5 ± 2.9) and approximately 19% with respect to normalized path length (1.8 ± 0.04 versus 1.4 ± 0.03). Fig. 5 shows that in the case of HARDI, clustering and path length is approximately 97% and 11%, respectively, greater for a 4000-node template compared to the AAL. All these discrepancies between HARDI and DTI were found to be statistically significant. Specifically, for all the nodal scales considered, each of the following null hypotheses was rejected with $p < 10^{-4}$: $\gamma_{HARDI} = \gamma_{DTI}$, $\lambda_{HARDI} = \lambda_{DTI}$, $l_{G;HARDI} = l_{G;DTI}$ and $c_{G;HARDI} = c_{G;DTI}$. A two-tailed Student's t-test was used to assess statistical significance, where the standard deviation used to compute this t-test quantified the variation of each measure over parcellations of the same scale.

The next measure considered was global network efficiency (Latora and Marchiori, 2001), which is inversely related to path length. Fig. 7 shows efficiency plotted as a function of the number of nodes and demonstrates efficiency decreases as nodal scale is made finer. HARDI yielded a marginally more efficient network than DTI. In particular, the null hypothesis of equal network efficiency for HARDI and DTI was rejected with $p < 10^{-8}$ for all the nodal scales considered. The higher efficiency of HARDI may be due to the greater proportion of long range connections (e.g. transcallosal fibers evident in Fig. 3) identified with HARDI, which serve to shorten average path lengths. Another explanation stems from the fact that slightly more nodes were disconnected from the giant component in DTI, although no case was encountered where more than 3% of all nodes were disconnected. Disconnected nodes were assigned an efficiency of zero, thereby reducing the average efficiency estimate. Efficiency obeys the same trends that have already been explicated with respect to clustering and path length; namely, variation in efficiency across parcellations of the same scale is rather small, however, variation across different scales is much greater. Indeed, for any pair of nodal scales that was considered, the discrepancy in the values of small-worldness, global efficiency and normalized clustering coefficient between the pair was significant ($p < 0.01$). The same can be said of the normalized path length, except the discrepancy between the 1000 and 2000, and 2000 and 3000 nodal scales was not significant for this particular measure.

To test for scale-freeness, degree rank was plotted as a function of degree on a doubly logarithmic axis. This plot is shown for HARDI and DTI in Fig. 8, where a separate trace is shown for $N = $ AAL, 500, 2000 and 4000 nodes. For all the scales considered, linearity is evident in Fig. 8 for low degrees; however, a tail-off is also apparent for high degrees. This suggests anatomical brain networks are not scale-free, but rather heavy-tailed.
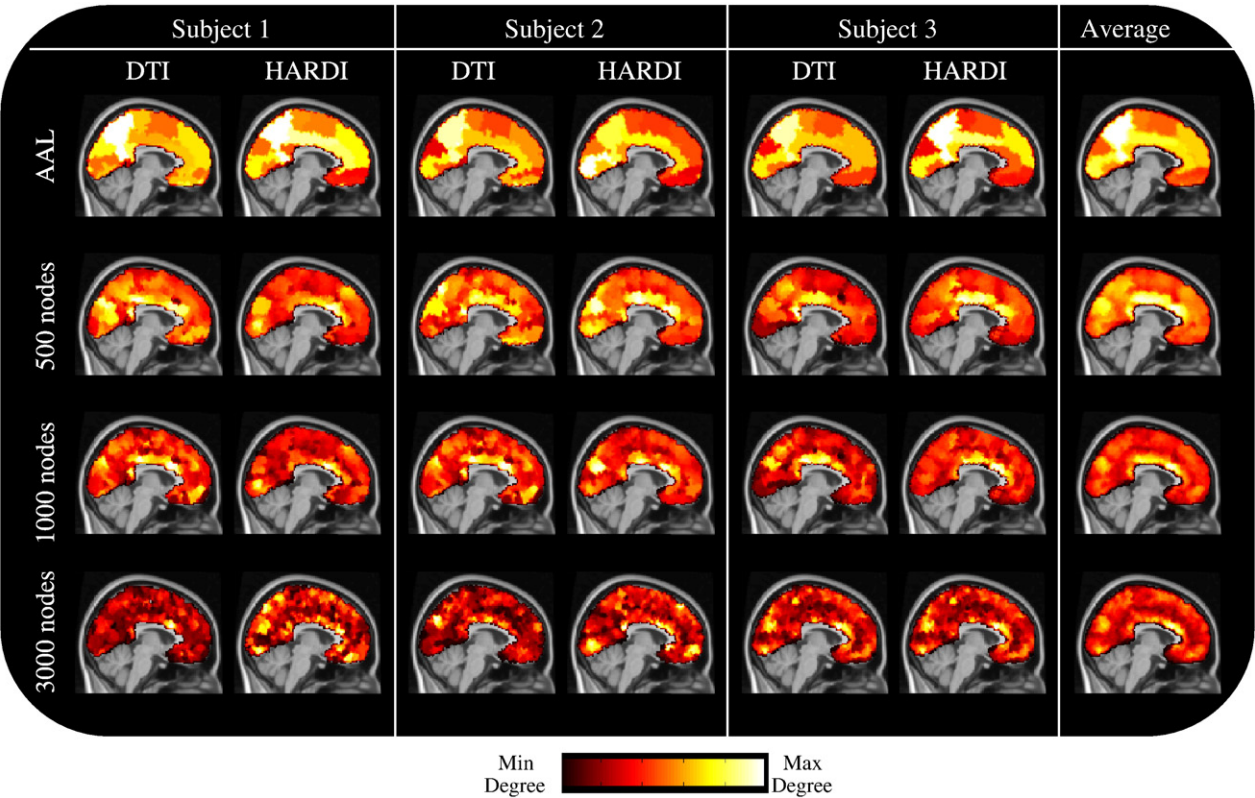

Fig. 9. Nodal degree ($x = 4$ mm MNI).

To further investigate degree scaling, each empirical degree distribution shown in Fig. 8 was fitted to three distinct models: a power law, $y_i = c_{di}^{-\alpha}$; an exponential, $y_i = ce^{-\alpha d_i}$; and, an exponentially truncated power law, $y_i = cd_i^{\alpha-1}e^{-d_i/k}$, where d_i and y_i are the degree of the ith node and complementary distribution function, respectively. Note that each of these models can be linearized by taking the logarithm of both sides. Hence, the empirical data could be fitted to each model using least squares. Goodness-of-fit was compared using the deviance of the fit at the computed solution as well as Akaike's information criterion. Of the three models considered, the exponentially truncated power law consistently yielded the best fit for both HARDI and DTI, and for all the scales considered. In particular, the exponentially truncated power law never yielded less than a 70% better fit than the other two models, while the deviance of the fit never exceeded 2. Table 3 tabulates the least squares fit of the three parameters underlying the exponentially truncated power law model. Note that the cut-off degree, k, is higher for HARDI for all the scales considered.

For each of the measures considered, Table 4 tabulates the expected difference (relative error) between the values of a measure computed by two experimenters who follow precisely the same methodology and use the same data set, but employ different parcellations of the *same* scale. The purpose of this is to quantitatively answer: to what extent will the two experimenters appear to be in error with each other due to the use of different parcellation templates of the same scale? In other words, Table 4 quantifies the size of the confidence intervals shown in Figs. 4 and 5. Relative errors were computed with the permutation based approach described in Section 2.6. Note that since the AAL template is fixed, its relative error is zero.

Table 4 shows that the maximum discrepancy between the two experimenters never exceeds 3% for any of the measures. Path length is the least sensitive to parcellation differences, while small-worldness and clustering offer roughly the same stability. Since the parcellation scheme employed herein was constrained by the AAL, in the sense that each node was required to lie within one and only one AAL region-of-interest, the discrepancies reported in Table 4 may be smaller compared to a non-constrained parcellation scheme. We implemented a non-constrained parcellation scheme (i.e. nodes were permitted to lie across multiple AAL regions-of-interest) and can report that the maximum discrepancy increased to approximately 16% for small-worldness and clustering, and approximately 4% for path length.

Finally, some local measures were considered; namely, nodal degree and betweenness centrality. The presentation and interpretation of a local measure is more intricate because a separate value must be considered for each of possibly thousands of nodes.

Fig. 9 shows a sagittal representation of nodal degree at slice $x = 4$ mm of MNI space. The four rows correspond to parcellations of scale 82 (AAL), 500, 1000 and 3000 nodes. Each of the 6 acquisitions (DTI and HARDI in each of 3 subjects) is represented by a separate column, while the last column corresponds to the average over all acquisitions. For each of the non-AAL cases, each slice is the average over 100 random parcellations. For example, the slice shown in row 2, column 1, corresponds to the average over 100 random parcellations of scale $N = 500$ for DTI in subject 1, while the slice shown in row 2, column 7, corresponds to the grand average over each of the 6 acquisitions and over each of the 100 random parcellations for each of the 6 acquisitions.

Fig. 9 reveals that the nodes of highest degree are located in the cingulate cortex and to a lesser extent in the parietal/occipital lobe. Previous diffusion-MRI studies have also reported strong anatomical connectedness of the cingulate. For example, Beckmann et al., 2009 segmented the cingulate cortex into 9 subregions based on its connectivity profile with 11 target regions, including the hippocampus, amygdala, orbitofrontal, parietal, precentral and prefrontal cortex.

In Fig. 9, the strong connectedness of the cingulate is most apparent for the 500 and 1000-node parcellations; however, the
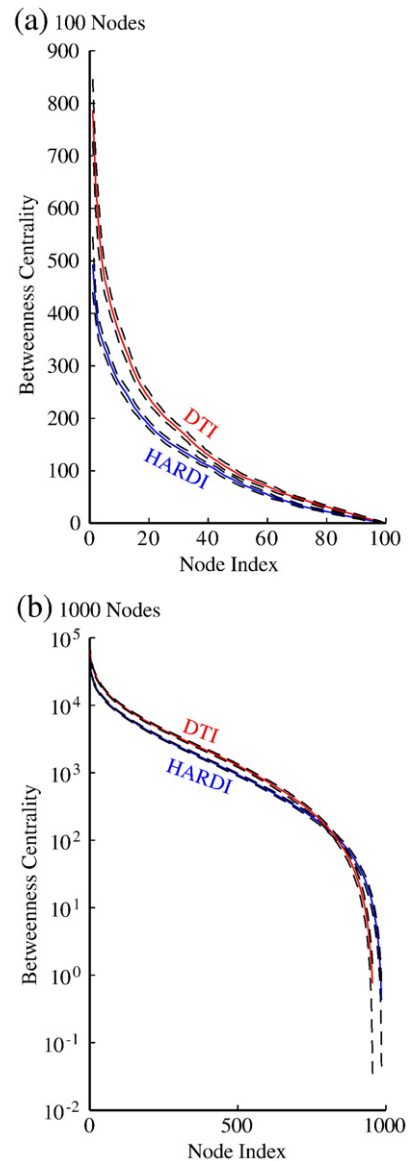

Fig. 10. Nodal betweenness centrality.

presence of the cingulate is not striking in the case of the AAL, while only the anterior cingulate is apparent for the 3000-node case. This suggests nodal degree exhibits strong dependence on parcellation scale.

Fig. 10 shows the distribution of nodal betweenness centrality for the cases of 100 and 1000 nodes. Nodes have been sorted such that the node exhibiting the highest centrality is labeled one, while the node exhibiting the lowest centrality is labeled N. A node that exhibits a large betweenness centrality indicates that it is traversed by the shortest interconnecting path for many node pairs. Fig. 10 shows betweenness centrality is marginally higher for DTI relative to HARDI, although a crossover point is evident in Fig. 10b. DTI exhibits higher betweenness centrality due to longer path lengths. In particular, the longer paths for DTI traverse more nodes than their shorter HARDI counterparts, thereby resulting in higher betweenness centrality.

Discussion and conclusions

In most natural and engineered networks, what constitutes a node and what constitutes a link is clear and well-defined. For example, in

social networks, nodes represent individuals (or organizations), while links represent relationships, friendships, etc. When the Internet is modeled as a network, nodes represent computers (or routers), while links represent the wiring and optical fibers that interconnect them. In food webs, nodes represent particular species of animal, while links represent predator/prey relationships.

In macroscopic human brain imaging data, the best definition of a node is unclear. As a consequence, experimenters have used a variety of template-based definitions, each varying with respect to the size, location, definitional criteria and number of nodes specified. In particular, inter-study variations in the number of nodes analyzed have been of several orders of magnitude, raising a basic question of comparability.

This raises a basic question of comparability and consistency across studies. Specifically: what is the dependency of various network properties on nodal definition and parcellation scale, given the lack of a standard parcellation template or scale. The purpose of this paper was to quantify the extent of dependency of several local and global topological properties on: scale (i.e. number of nodes), parcellation (i.e. location of borders separating nodes) as well as the acquisition protocol and tractographic method (i.e. HARDI-based tractography accounting for crossing fibers versus DTI-based stream-line tractography).

The results presented herein are most easily understood in the context of two experimenters who seek to uncover the topological properties of a diffusion-MRI derived brain network. It was shown if both experimenters use distinct parcellations of the *same* scale, the values of small-worldness (σ-ratio), clustering coefficient and path length reported by the two experimenters will not be discrepant by more than 3%. This assumes both experimenters use a *random* parcellation template constructed using a scheme akin to the one devised herein. It was not investigated whether this discrepancy remains for two different parcellations constructed using distinct *anatomical* criteria, primarily due to the lack of fine-grained anatomically-driven parcellations. As shown in Table 1, previous studies investigating scales beyond 100 nodes have predominantly utilized random parcellations. The discrepancy found between parcellations may be attributable to a single node that artificially combines several functionally/anatomically distinct grey-matter regions into a single entity (as exemplified by the example introduced earlier in Fig. 1), or two nodes that artificially subdivide a unitary functional region.

Suppose now the first experimenter uses a 4000-node template, while the second experimenter uses the AAL template. This situation roughly exemplifies the studies of Achard et al., 2006 versus Van den Heuvel et al., 2008 (90 nodes versus 10^4 nodes). In this case, the discrepancy in value of small-worldness reported by the two experimenters increased to about 95% on average. This discrepancy is indeed consistent with the σ-ratios reported in Achard et al., 2006 and Van den Heuvel et al., 2008, although it must be remembered that these studies considered rs-fMRI networks. Specifically, Achard et al., 2006 (90 nodes) reported σ-ratios in the range 1.42–2.30, depending on the wavelet scale, while Van den Heuvel et al., 2008 (10^4 nodes) reported σ-ratios as high as about 45 for the sparsest network configurations. Discrepancies of a similar magnitude were found in this situation for the other global measures considered.

Finally, suppose the first experimenter now acquires his/her data with a HARDI protocol (252 gradient directions), which enables him/her to fit an ODF to each voxel and thereby model multiple axonal orientations. Meanwhile, the second experimenter persists with 60 gradient directions, a 50% weaker diffusion gradient ($b = 2000$ s/mm^2) and fits a single-compartment Gaussian diffusion profile to each voxel. In this case, the discrepancy in the value of small-worldness reported by the two experimenters was negligible at the coarsest scales considered, but increased to about 13% for a scale of 4000 nodes. At a scale of 4000 nodes, the discrepancy in the values of
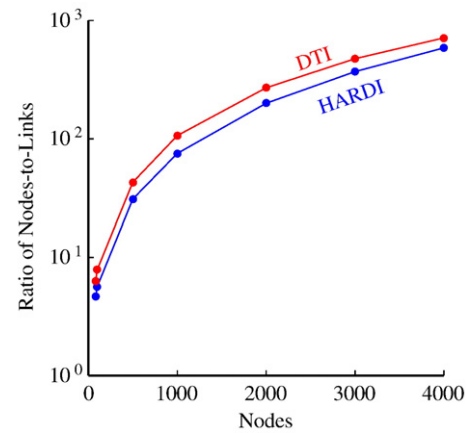

Fig. 11. Connection sparsity (ratio of the number of nodes-to-links) as a function of the parcellation scale. Values plotted are averages across the three subjects.

clustering and path length was 31% and 19%, respectively. This discrepancy is solely attributable to the differences in the acquisition protocol and tractographic algorithm.

It was observed that finer parcellation scales resulted in stronger small-world attributes (i.e. larger σ-ratio, albeit a slightly longer average path length), due to a disproportionate increase in the clustering coefficient. There are several possible reasons for this disproportionate increase in clustering at finer scales. The most likely explanation is that networks of finer scale are inherently more sparse, and thus exhibit increased clustering due to this greater sparsity. In Fig. 11, sparsity (ratio of nodes-to-links) is plotted as a function of scale. Note that in rs-fMRI networks, the σ-ratio has been shown to increase as sparsity is increased; in particular, as links representing weak functional correlations are excluded (e.g. see Fig. 4 in Van den Heuvel et al., 2008).

Another possibility is that this may be an intrinsic property of small-world networks. As the size of the network increases, a greater proportion of connections may be local, as only a few long-range connections are required to produce a dramatic reduction in mean path length. Other possible explanations implicate technical reasons. For example, it may be that the smaller size of a node at finer scales makes it less likely that it will be connected by a long-range connection. Alternatively, increased clustering at finer scales may arise because the average distance between neighboring nodes becomes smaller, making it more likely that they are connected.

To eliminate any potential effects driven exclusively by the sparsity variation found across different scales (see Fig. 11), we could have forced all networks to match the sparsity of the sparsest networks analyzed, which were the 4000-node cases. This would involve eliminating the weakest links (i.e. those comprising the fewest number of streamlines) one at a time until sparsity reaches the value of the most sparse network. Therefore, all network scales would be matched with respect to sparsity, thereby precluding effects owing to sparsity variation. However, we did not implement this approach because this is not what happens in practice. Since d-MRI networks are intrinsically sparse (unlike their rs-fMRI counterparts), an experimenter has no need to eliminate any links. Indeed, the process of eliminating links is rather unjustified, unless the links are known to be spurious, and can be viewed as artificially forcing a network from its natural sparsity level to match an arbitrarily chosen sparsity threshold. We therefore opted to analyze all networks at their intrinsic sparsity. In doing so, we have assumed effects owing to sparsity variation are not artefact, but rather natural topological differences.

Local topological attributes were investigated by calculating the degree of each node. Nodes with highest degree, corresponding to

network hubs, were identified in medial frontal and parietal areas, and to a lesser extent, lateral fronto-temporal regions. A similar pattern has been observed by others, suggesting these regions may comprise a structural core of anatomical connectivity (Hagmann et al., 2008). This pattern was broadly conserved across scales, although regional heterogeneity was reduced at finer scales. The spatial patterns observed with HARDI and DTI were again broadly consistent, although more high degree nodes were identified particularly on the lateral surface with the HARDI acquisition.

The results presented herein suggest that both local and global topological properties of human brain networks exhibit strong dependence on the choice of parcellation scale. It is important to emphasize that this strong dependence does not suggest a given parcellation scale is any more "optimal" than another.

A critical question that remains is: What parcellation scale should the experimenter employ? This question should be settled with consideration of several pragmatic issues. In particular, the experimenter should employ a sufficiently fine parcellation scale in order to mitigate template-driven dependencies; however, several practical considerations preclude the use of arbitrarily fine scales. As the parcellation scale is made finer, the volume (or surface area) encapsulated by each node is reduced, and thus the probability that a streamline intersects this volume approaches zero. A node that is not intersected by any streamlines remains disconnected from the network. And if only a few streamlines intersect each node, a noisy connectivity matrix is likely to result because whether or not a pair of nodes is connected wholly depends on the existence of a few streamlines. A potential solution is to increase the number of streamlines initiated when considering finer scales; however, this introduces additional computational burden. In the case of rs-fMRI networks, a reduction in nodal scale results in a reduction in the SNR of the time series at each node, which in turn adds noise to the connectivity matrix. This is because the time series at each node is derived as an average across all voxels composing the node.

While the focus herein was on modeling macroscopic connectivity in the human brain, it should be recognized that the first brain networks to be characterized as a graph were in fact microscopic; in particular, the entire nervous system of the nematode *Caenorhabditis elegans* was mapped with electron microscopy (Achacoso and Yamamoto, 1992) and analyzed as a graph (White et al., 1986). For this case, the choice of nodes was obvious: individual neurons correspond to nodes, while links characterize axons. The issue of nodal choice first arose when brain networks of mammalia such as the cat and macaque were analyzed (Felleman and Van Essen, 1991; Hilgetag et al., 2000a,b; Sporns et al., 2007; Young, 1993).

This study utilized FACT streamline tracking (Mori et al., 1999) to perform tractography. The FACT algorithm is simple, robust, computationally inexpensive and arguably the most ubiquitous tracking algorithm in use today. These four factors were the key determinant in the choice of tracking algorithm in this study.

However, it is important to remark that streamline tracking is not without its limitations. For example, local greediness is one such limitation that has been shown to obstruct the reconstruction of long distance connections (Zalesky, 2008). A streamline can be irrecoverably steered off-course if it traverses a region at which there is some uncertainty in the direction of propagation, either due to partial volume effects, a poor fit of the diffusion tensor (DTI) or ODF (HARDI), or simply due to noise. The longer a streamline, the greater the probability of encountering this kind of local uncertainty.

This limitation, among others, has motivated the development of new tractographic methods founded on novel concepts such as shortest paths in a graph (Itturia-Medina et al., 2008a), maximum flow in a graph (Zalesky and Fornito, 2009), Navier–Stokes fluid flow (Hageman et al., 2009) and global parametrization of connections (Jbabdi et al., 2007). These methods were not investigated in this

study. Seeding probabilistic streamlines (Behrens et al., 2003; Behrens et al., 2007) from each node is yet another alternative.

In this study, a common set of streamline termination criteria were used for both HARDI and DTI tractography; otherwise, it could not
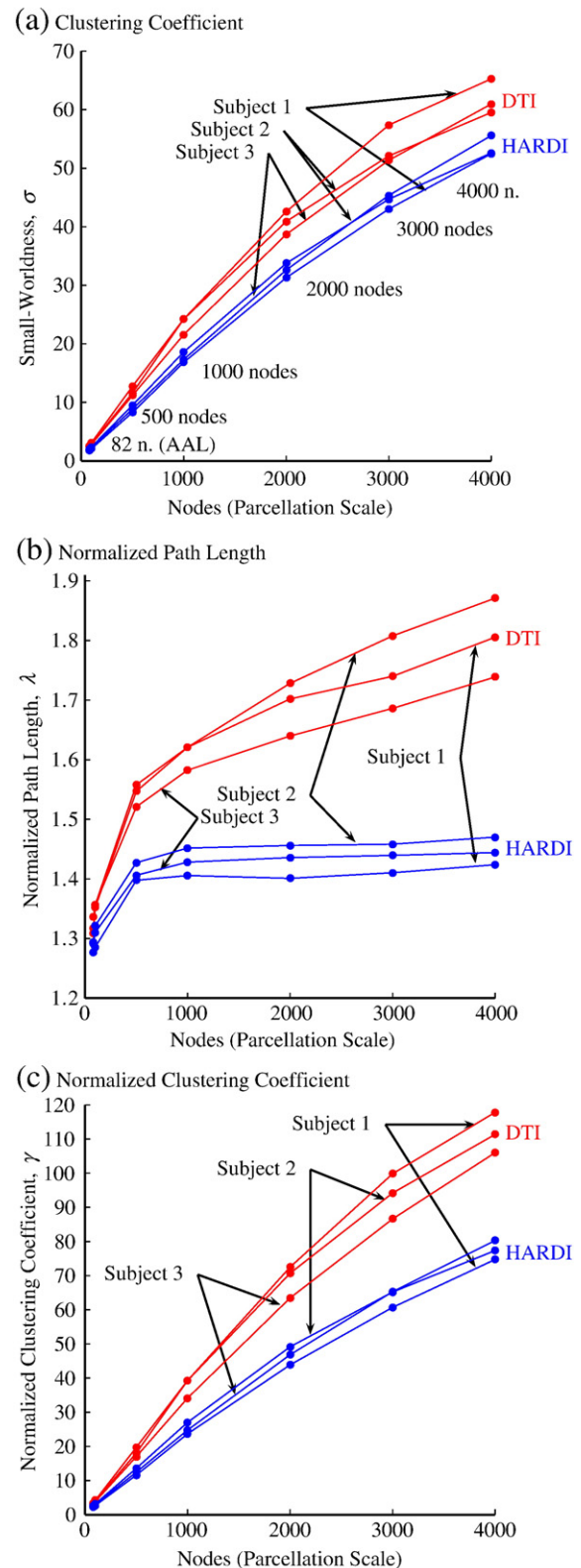
Fig. 12. σ, λ and γ plotted as a function of the total number of nodes, where a separate trace is shown for each subject and acquisition (HARDI and DTI in each of 3 subjects).

have been ruled out that any discrepancies found between the two acquisitions were solely attributable to different termination criteria. If the termination criteria for HARDI were instead based on *generalized* FA (Tuch, 2004), the discrepancies found between HARDI and DTI may have been greater, due to the potential reduction in the risk of HARDI streamlines terminating prematurely.

Macroscopic network models of the human brain have been analyzed over a wide range of nodal scales, a variety of parcellation templates, different acquisition protocols as well as tractographic methods tailored to these protocols. It is important to recognize that topological attributes of these networks exhibit strong dependence on these parameters, especially nodal scale. As such, it is critical that a reported σ-ratio (small-worldness), clustering coefficient, etc. is considered with respect to a particular scale and parcellation template. This paper *quantified* the expected discrepancy in the value of several topological measures that would arise across studies employing disparate nodal scales, parcellation templates and tractographic algorithms.

An investigation of the inter-subject variability of anatomical network measures may be a fruitful avenue along which this study could be extended and would complement the work of Deuker et al., 2009 in which inter-subject variability was examined in functional network models derived from MEG data.

Acknowledgments

Appendix 1

Appendix A1: Parcellation algorithm pseudocode

Algorithm 1 was invoked to generate random parcellations of grey-matter comprising N contiguous nodes. Each node was constrained to lie within one and only one AAL region-of-interest. This constraint precluded formation of nonsensical nodes, such as those that span both hemispheres or multiple, anatomically distinct regions. The number of nodes (i.e. proportion of N) designated to an AAL ROI was proportional to the total number of streamline endpoints residing in that ROI.

Algorithm 1 Generate a random, voxel-based parcellation of grey-matter comprising N contiguous nodes. Each resulting node is confined to boundaries of precisely one AAL region-of-interest (ROI).

Inputs:

- A_n denotes a set of voxels composing nth AAL ROI, where $n = 1,...,82$;
- $p_n < 1$ denotes the proportion of streamline endpoints residing in the nth AAL ROI (tractography output);
- N denotes desired number of nodes.

Outputs:

- J_n denotes the number of nodes into which the nth AAL ROI subdivided;
- $G_n(j)$ denotes set of voxels composing jth node of nth AAL ROI, where $n = 1,..., 82$ and $j = 1,..., J_n$.

```
1: for n = 1, 2, . . . , 82 do
2:     J_n := ⌊p_n N⌋
3:     {G_n(j)}^{J_n}_{j=1} := parcellate_AAL_ROI(J_n, A_n)
4: end for
5: return G_n(j), ∀n = 1,..., 82; ∀j = 1,..., J_n
```

```
1: subroutine: parcellate AAL_ROI_(J,A) ≡
2: for j = 1, 2,..., J do
3:     Randomly choose a voxel from A. Let x ∈ A be that voxel.
4:     A ← A − {x}
5:     G(j) := {x}
6: end for
7: 𝒥 := {1, 2,..., J}
8: while A ≠ ∅ do
9:     j* := arg min_{j∈𝒥} {|G(j)|}
10:    if exists at least one voxel in A that neighbors at least one voxel
       in G(j*) then
11:        Determine which voxel in A is the closest neighbor of
           G(j*). Let x ∈ A be that voxel.
12:        G(j*) ← G(j*) + {x}
13:        A ← A − {x}
14:    else
15:        𝒥 ← 𝒥 − {j*}
16:    end if
17: end while
18: return {G(j)}^{J}_{j=1}.
```

After Algorithm 1 has terminated, note that $\sum_{n=1}^{82} J_n \leq N$. That is, the final number of nodes, $\sum_{n=1}^{82} J_n$, may be slightly less than the requested number of nodes N. If this is of concern, set $J_{n^*} := J_{n^*} + 1$, where n^* is randomly chosen from $\{1,...,82\}$, and repeat $N - \sum_{n=1}^{82} J_n$ times.

The term 'closest neighbor' in Algorithm 1 refers to the voxel $\mathbf{x} \in A$ that shares the greatest surface area (i.e. most voxel faces) with a voxel in node $G(j^*)$. If two or more voxels in A are equally closest neighbors, the voxel that is closest in distance to the current center of mass of $G(j^*)$ is chosen. Any further ties between voxels are broken randomly.

At any given iteration, J is a set containing the index of each node that can be enlarged during a subsequent iteration. That is, any node that does *not* appear in J cannot be enlarged, since it does not have any neighbors in A.

The while loop in Algorithm 1 is guaranteed to terminate as long as A is contiguous. For the purposes of Algorithm 1, contiguity was defined using the usual 26-voxel neighborhood.

Appendix 2: inter-subject variability

In Figs. 4 (σ vs. nodal scale) and 5 (λ and γ vs. nodal scale), the means and standard deviations of each measure were averaged across the 3 DTI acquisitions (each acquisition corresponding to a different subject) and separately across the 3 HARDI acquisitions, thereby yielding two data points (blue and red) for each nodal scale. To investigate the inter-subject variability of σ, λ and γ, Fig. 12 shows the equivalent of Figs. 4 and 5, but with a separate trace plotted for each of the 6 acquisitions. That is, averaging was not performed over the three subjects.

References

Achacoso, T.B., Yamamoto, W.S., 1992. AY's Neuroanatomy of C. Elegans for Computation. CRC Press.

Achard, S., Bullmore, E., 2007. Efficiency and cost of economical brain functional networks. PLoS Comput. Biol. 3, e17.

Achard, S., Salvador, R., Whitcher, B., Suckling, J., Bullmore, E., 2006. A resilient, low frequency, small-world, human brain functional network with highly connected association cortical hubs. J. Neurosci. 4 (1), 63–72.

Albert, R., Jeong, H., Barabasi, A.-L., 2000. Error and attack tolerance of complex networks. Nature 406, 378–382.

Alemán-Gómez Y., Melie-García L., Valdes-Hernández P., 2006. IBASPM: Toolbox for automatic parcellation of brain structures. Presented at the 12th Annual Meeting of the Organization for Hum Brain Mapp. June 11-15. 2006. Florence. Italy.

Amaral, L.A.N., Scala, A., Barthelemy, M., Stanley, H.E., 2000. Classes of small-world networks. PNAS 97 (21), 11149–11152.

Bassett, D.S., Meyer-Lindenberg, A., Achard, S., Duke, T., Bullmore, E., 2006. Adaptive reconfiguration of fractal small-world human brain functional networks. PNAS 103 (51), 19518–19523.

Bassett, D.S., Bullmore, E., Verchinski, B.A., Mattay, V.S., Weinberger, D.R., Meyer-Lindenberg, A., 2008. Hierarchical organization of human cortical networks in health and schizophrenia. J. Neurosci. 28 (37), 9239–9248.

Bayati, M., Han, J., Saberi, A., 2007. A sequential algorithm for generating random graphs. LNCS 4627, 326–340.

Beckmann, M., Johansen-Berg, H., Rushworth, M.F.S., 2009. Connectivity-based parcellation of human cingulate cortex and its relation to functional specialization. J. Neurosci. 29 (4), 1175–1190.

Behrens, T.E., Woolrich, M.W., Jenkinson, M., Johansen-Berg, H., Nunes, R.G., Clare, S., Matthews, P.M., Brady, J.M., Smith, S.M., 2003. Characterization and propagation of uncertainty in diffusion-weighted MR imaging. Magn. Reson. Med. 50, 1077–1088.

Behrens, T.E., Berg, H.J., Jbabdi, S., Rushworth, M.F., Woolrich, M.W., 2007. Probabilistic diffusion tractography with multiple fibre orientations: what can we gain. NeuroImage 34, 144–155.

Bullmore, E., Sporns, O., 2009. Complex brain networks: graph theoretical analysis of structural and functional systems. Nat. Rev. Neurosci. 10, 186–198.

Bullmore, E., Barnes, A., Bassett, D.S., Fornito, A., Kitzbichler, M., Meunier, D., Suckling, J., 2009. Generic aspects of complexity in brain imaging data and other biological systems. NeuroImage 47 (3), 1125–1134.

Collins, D.L., Holmes, C.J., Peters, T.M., Evans, A.C., 1995. Automatic 3-D model-based neuroanatomical segmentation. Hum. Brain Mapp. 3, 190–208.

Deuker, L., Bullmore, E., Smith, M., Christensen, S., Nathan, P.J., Rockstroh, B., Basset, D.S., 2009. Reproducibility of graph metrics of human brain functional networks. NeuroImage 47 (4), 1460–1468.

Eguiluz, V.M., Chialvo, D.R., Cecchi, G.A., Baliki, M., Apkarian, A.V., 2005. Scale-free brain functional networks. Phy. Rev. Lett. 94 (1), 018102.

Felleman, D.J., Van Essen, D.C., 1991. Distributed hierarchical processing in the primate cerebral cortex. Cereb. Cortex 1, 1–47.

Freeman, L.C., 1979. Centrality in social networks conceptual clarification. Social Networks 1 (3), 215–239.

Gong, G., He, Y., Concha, L., Lebel, C., Gross, D.W., Evans, A.C., Beaulieu, C., 2009. Mapping anatomical connectivity patterns of human cerebral cortex using in vivo diffusion tensor imaging tractography. Cereb. Cortex 9, 524–536.

Hageman, N.S., Toga, A.W., Narr, K.L., Shattuck, D.W., 2009. A diffusion tensor imaging tractography algorithm based on Navier–Stokes fluid mechanics. IEEE Trans. Med. Imag. 28 (3), 348–360.

Hagmann, P., Kurant, M., Gigandet, X., Thiran, J.-P., Wedeen, V.J., Meuli, R., Thiran, J.P., 2007. Mapping human whole-brain structural networks with diffusion MRI. PLoS ONE 2 (7), e597.

Hagmann, P., Cammoun, L., Gigandent, X., Meuli, R., Honey, C.J., Wedeen, V.J., Sporns, O., 2008. Mapping the structural core of the human cerebral cortex. PLoS Biol. 6 (7), e159.

He, Y., Chen, Z.J., Evans, A.C., 2007. Small-world anatomical networks in the human brain revealed by cortical thickness from MRI. Cereb. Cortex 17, 2407–2419.

He, Y., Chen, Z.J., Evans, A.C., 2008. Structural insights into aberrant topological patterns of large-scale cortical networks in Alzheimer's disease. J. Neurosci. 28 (18), 4766–5756.

He, Y., Dagher, A., Chen, Z., Charil, A., Zijdenbos, A., Worsley, K., Evans, A.C., 2009. Impaired small-world efficiency in structural cortical networks in multiple sclerosis associated with white matter lesion load. Brain 132 (12), 3366–3379.

Hess, C.P., Mukherjee, P., Han, E.T., Xu, D., Vigneron, D.B., 2006. Q-ball reconstruction of multimodal fiber orientations using the spherical harmonic basis. Magn. Res. Med. 56 (1), 104–117.

Hilgetag, C.C., Burns, G.A., O'Neill, M.A., Scannell, J.W., Young, M.P., 2000a. Anatomical connectivity defines the organization of clusters of cortical areas in the macaque monkey and cat. Phil. Trans. R. Soc. Lond. B. Biol. Sci. 355, 91–110.

Hilgetag, C.C., O'Neill, M.A., Young, M.P., 2000b. Hierarchical organization of macaque and cat cortical sensory systems explored with a novel network processor. Phil. Trans. R. Soc. Lond. B. Biol. Sci. 355, 71–89.

Honey, C.J., Sporns, O., Cammoun, L., Gigandet, X., Thiran, J.-P, Meuli, R., Hagmann, P., 2009. Predicting human resting-state functional connectvity from structural connectivity. PNAS 106 (6), 2035–2040.

Itturia-Medina, Y., Canales-Rodríguez, E.J., Melie-García, L., Valdés-Hernández, P.A., Matínez-Montes, E., Alemán-Gómez, Y., Sánchez-Bornot, J.M., 2008a. Characteri-zing brain anatomical connections using diffusion weighted MRI and graph theory. NeuroImage 36 (3), 645–660.

Itturia-Medina, Y., Sotero, R.C., Canales-Rodríguez, E.J., Alemán-Gómez, Y., Melie-García, L., 2008b. Studying the human brain anatomical network via diffusion-weighted MRI and graph theory. NeuroImage 40 (3), 1064–1076.

Jbabdi, S., Woolrich, M.W., Anderson, J.L.R., Behrens, T.E.J., 2007. A Bayesian framework for global tractography. NeuroImage 37, 116–129.

Jenkinson, M., Bannister, P.R., Brady, J.M., Smith, S.M., 2002. Improved optimisation for the robust and accurate linear registration and motion correction of brain images. NeuroImage 17 (2), 825–841.

Kaiser, M., Hilgetag, C.C., 2006. Nonoptimal component placement, but short processing paths, due to long-distance projections in neural systems. PLoS Comput. Biol. 2 (7), e95.

Kaiser, M., Martin, R., Andras, P., Young, M.P., 2007. Simulation of robustness against lesions of cortical networks. Eur. J. Neurosci. 25, 3185–3192.

Latora, V., Marchiori, M., 2001. Efficient behavior of small-world networks. Phys. Rev. Lett. 87 (19), 198701.

Liu, L., Alderson, D., Doyle, J.C., Willinger, W., 2005. Towards a theory of scale-free graphs: definitions, properties and implications. Internet Mathematics 2 (4), 431–523.

Liu, Y., Liang, M., Zhou, Y., He, Y., Hao, Y., Song, M., Yu, C., Liu, H., Liu, Z., Jiang, T., 2008. Disrupted small-world networks in schizophrenia. Brain 131, 945–961.

Maslov, S., Sneppen, K., 2002. Specificity and stability in topology of protein networks. Science 296, 910–913.

Micheloyannis, S., Pachou, E., Stam, C.J., Vourkas, M., Erimaki, S., Tsirka, V., 2006. Using graph theoretical analysis of multi-channel EEG to evaluate the neural efficiency hypothesis. Neurosci. Lett. 402, 273–277.

Mori, S., Crain, B.J., Chacko, V.P., Van Zijl, P.C., 1999. Three-dimensional tracking of axonal projections in the brain by magnetic resonance imaging. Ann. Neurol. 45 (2), 265–269.

Newman, M.E.J., 2003. The structure and function of complex networks. SIAM Rev. 45, 167–256.

Park, C.-H., Kim, S.Y., Kim, Y.-H., Kim, K., 2008. Comparison of the small-world topology between anatomical and functional connectivity in the human brain. Physica A 387, 5958–5962.

Salvador, R., P na, A., Menon, D.K., Adrian Carpenter, T., Pickard, J.D., Bullmore, E., 2005a. Formal characterization and extension of the linearized diffusion tensor model. Hum. Brain Mapp. 24, 144–155.

Salvador, R., Suckling, J., Coleman, M.R., Pickard, J.D., Menon, D., Bullmore, E., 2005b. Neurophysiological architecture of functional magnetic resonance images of human brain. Cereb. Cortex 15, 1332–1342.

Salvador, R., Suckling, J., Schwarzbauer, C., Bullmore, E., 2005c. Undirected graphs of frequency-dependent functional connectivity in whole-brain networks. Philos. Trans. R. Soc. Lond. B. Biol. Sci. 360, 937–946.

Skudlarski, P., Jagnnathan, K., Calhoun, V.D., Hampson, M., Skudlarska, B.A., Pearlson, G., 2008. Measuring brain connectivity: Diffusion tensor imaging validates resting state temporal correlations. NeuroImage 43, 554–561.

Sporns, O., Chialvo, D.R., Kaiser, M., Hilgetag, C.C., 2004. Organization, development and function of complex brain networks. Trends Cogn. Sci. 8 (9), 418–425.

Sporns, O., Tononi, G., Kötter, R., 2005. The human connectome: a structural description of the human brain. PLoS Comput. Biol. 1 (4), e42.

Sporns, O., Honey, C.J., Kötter, R., 2007. Identification and classification of hubs in brain networks. PLoS ONE 2, e1049.

Stam, C.J., 2004. Functional connectivity patterns of human magnetoencephalographic recordings: a 'small-world' network. Neurosci. Lett. 355 (2004), 25–28.

Stam, C.J., Jones, B.F., Nolte, G., Breakspear, M., Scheltens, P., 2007. Small-world networks and functional connectivity in Alzheimer's disease. Cereb. Cortex 17, 92–99.

Tournier, J.-D., Calamante, F., Gadian, D.G., Connelly, A., 2005. Direct estimation of the fiber orientation density function from diffusion-weighted MRI data using spherical deconvolution. NeuroImage 23, 1176–1185.

Tuch, D., 2004. Q-ball imaging. Magn. Reson. Med. 52 (6), 1358–1372.

Tzourio-Mazoyer, N., Landeau, B., Papathanassiou, D., Crivello, F., Etard, O., Delcroix, N., Mazoyer, B., Joliot, M., 2002. Automated anatomical labeling of activations in SPM using a macroscopic anatomical parcellation of the MNI MRI single-subject brain. NeuroImage 15 (1), 273–289.

Van den Heuvel, M.P., Stam, C.J., Boersma, M., Hulshoff Pol, H.E., 2008. Small-world and scale-free organization of voxel-based resting-state functional connectivity in the human brain. NeuroImage 43, 528–539.

Wang, J., Wang, L., Zang, Y., Yang, H., Tang, H., Gong, Q., Chen, Z., Zhu, C., He, Y., 2009a. Parcellation-dependent small-world brain functional networks: a resting-state fMRI study. Hum. Brain Mapp. 30, 1511–1523.

Wang, C.P., Zhu, C., He, Y., Zang, Y., Cao, Q., Zhang, H., Zhong, Q., Wang, Y., 2009b. Altered small-world brain functional networks in children with attention-deficit/hyper-activity disorder. Hum. Brain Mapp. 30 (2), 638–649.

Watts, D.J., Strogatz, S.H., 1998. Collective dynamics of 'small-world' networks. Nature 393, 440–442.

White, J.G., Southgate, E., Thomson, J.N., Bremer, S., 1986. The structure of the nervous system of the nematode Caenorhabditis Elegans. Phil. Trans. R. Soc. Lond. B. Biol. Sci. 314 (1165), 1–340.

Young, M.P., 1993. The organization of neural systems in the primate cerebral cortex. Proc. R. Soc. Lond. B. Biol. Sci. 252, 13–18.

Zalesky, A., 2008. DT-MRI fiber tracking: a shortest paths approach. IEEE Trans. Med. Imag. 27 (10), 1458–1471.

Zalesky, A., Fornito, A., 2009. A DTI-derived measure of cortico-cortical connectivity. IEEE Trans. Med. Imag. 28 (7), 1023–1036.